Full paper

All roads lead to Rome: Sodiation of different-stacked SnS₂

Zhongtao Ma [a,1], Zhenpeng Yao [e,f,1], Yingchun Cheng [d,1], Xuyang Zhang [d], Bingkun Guo [a],
Yingchun Lyu [a], Peng Wang [a], Qianqian Li [a,*], Hongtao Wang [c,**], Anmin Nie [a,b,***],
Alán Aspuru-Guzik [e,f,g,h]

[a] Materials Genome Institute, Shanghai University, Shanghai, 200444, China
[b] Center for High Pressure Science, State Key Laboratory of Metastable Materials Science and Technology, Yanshan University, Qinhuangdao, 066004, China
[c] Center for X-mechanics, Zhejiang University, Hangzhou, 310027, China
[d] Key Laboratory of Flexible Electronics & Institute of Advanced Materials, Jiangsu National Synergetic Innovation Center for Advanced Materials, Nanjing Tech
University, 30 South Puzhu Road, Nanjing, 211816, China
[e] Department of Chemistry and Chemical Biology, Harvard University, 12 Oxford Street, Cambridge, MA, 02138, United States
[f] Department of Chemistry and Department of Computer Science, University of Toronto, Toronto, Ontario, M5S 3H6, Canada
[g] Vector Institute for Artificial Intelligence, Toronto, Ontario, M5S 1M1, Canada
[h] Canadian Institute for Advanced Research (CIFAR) Senior Fellow, Toronto, Ontario, M5S 1M1, Canada

ARTICLE INFO

ABSTRACT

Structural symmetry variations of two-dimensional materials may significantly affect their reaction process and kinetics with alkali ions. Here, SnS₂ with different structural symmetry is used as the target to be comparatively investigated the phase transition pathway and ionic diffusion upon (de)sodiation in sodium-ion batteries using *in situ* transmission electron microscopy and *ex situ* x-ray photoelectron spectroscopy in combination with first-principles calculations. Different intermediate phases, AA1 NaSnS₂ for trigonal SnS₂ and AB1 NaSnS₂ for hexagonal SnS₂, are observed after sodium ions fully occupy all O_h sites. While the coming conversion/alloying reaction processes are relatively similar. The AA1/AB1 NaSnS₂ sequentially transits to SnS, β-Sn and Na₁₅Sn₄ phases starting from T_d sites of SnS₂ being held. Reversible reactions occur among SnS, Na₁₅Sn₄ and Na₂Sₘ (2<m<8) in following cycles. Our works provide a deep understanding of the ionic diffusion and electrochemical reaction mechanisms for two-dimensional materials with different symmetry, and offer some guidance for the design of the high energy two-dimensional electrode materials.

1. Introduction

Sodium-ion batteries are promising energy storage techniques especially for large-scale renewable energy sources such as solar and wind because of their lower cost and relative abundance of Na [1,2]. Layered two-dimensional (2D) transition metal sulfides like tin sulfides (SnS₂) have drawn much attention due to its remarkable electrochemical capacity as anodes in sodium ion batteries [3,4]. The improving 2D transition metal sulfides anodes mainly demand a comprehensive understanding of their electrochemical reaction mechanisms and kinetics.

SnS₂ has a sandwich-like structure, consisting of two alternated hexagonally coordinated S planes and one sandwiched Sn planes. The layers interact with each other through weak van der Waals force, like MoS₂, which allows different stackings between layers, and enables diffusion channels for ions [5]. According to the distinct structural symmetry of adjacent layers, there are two different common polytypes of SnS₂: the trigonal P3̄m1 SnS₂ [6] and the hexagonal P6₃mc SnS₂ [7,8]. SnS₂ anode usually undergoes alkali ion insertion [9], conversion, and alloying as the sequence in the discharge process. Sooyeon Hwang et al. discovered two intermediate phases, *i.e.* layered Li$_x$SnS₂ and rock-salt Li$_y$SnS₂ before the conversion reaction, and then the intermediate phases convert to Li₂S and Sn after full lithiation [10]. Crystalline Sn nanoparticles are well arranged within an amorphous Li₂S "matrix", which leads to better electrochemical performance [11]. The structural

---

* Corresponding author.
** Corresponding author.
*** Corresponding author. Materials Genome Institute, Shanghai University, Shanghai, 200444, China.
  E-mail addresses: qianqianli@shu.edu.cn (Q. Li), htw@zju.edu.cn (H. Wang), anmin@ysu.edu.cn (A. Nie).
[1] These authors contributed equally to this work.

transformation of conversion/alloying-type electrodes usually significantly affect the electrochemical performance of the sodium ion batteries. However, the influence of structural symmetry of SnS_2 on the structural evolution remains elusive.

Here, we perform a comparative mechanistic study on the sodiation and desodiation processes of different structural symmetry of SnS_2, *i.e.* trigonal and hexagonal, using *in situ* TEM techniques in combination with the first-principles calculations. We are able to identify distinct intercalated intermediate AA1 $NaSnS_2$ and AB1 $NaSnS_2$ phases during the first sodiation of trigonal $P\overline{3}m1$ SnS_2 and hexagonal $P6_3mc$ SnS_2 respectively. Both of two SnS_2 are suffering anisotropic expansion phenomena along [001] and [100] upon Na insertion. After the first sodiation, these two kinds of SnS_2 electrodes show a similar conversion reaction between Na_2S and polysulfides, and reversible alloying reaction between SnS and $Na_{15}Sn_4$ during cycling. Meanwhile, these two phases exhibit similar electrochemical performance.

2. Material and methods

2.1. Synthesis of SnS_2 nanoplates

The procedures for synthesizing trigonal SnS_2 are listed as follows. Firstly, 1 mmol $SnCl_4 \cdot 5H_2O$ and 6 mmol thiourea were added to 20 ml deionized water. The mixed solution was subjected to mechanical stirring for 20 min. Then the obtained solution was placed in a 50 ml Teflon-lined autoclave and heated at 160 °C for 24 h. Finally, the precipitates were centrifuged and washed with deionized water and anhydrous ethanol for several times. The SnS_2 samples can be obtained after the final drying in a vacuum freeze drier for 5 h. For hexagonal SnS_2, the reagents are 1 mmol $SnCl_2 \cdot 2H_2O$ and 10 mmol thioacetamide instead of $SnCl_4 \cdot 5H_2O$ and thiourea, and the temperature of heating is 190 °C. The other procedures are as same as trigonal samples in exception of the extra purifying process (SnS_2 tends to agglomerate and precipitate, so this process involves several times by repeated rinsing and precipitating).

2.2. Structural and physical characterizations

The phase-structural composition of the products was characterized using powder X-ray diffraction (XRD, Cu Ka1 radiation, at 30 kV, Bruker). The details of the morphology were further characterized by transmission electron microscopy (TEM, JEOL 2100 TEM). The surface topography of the SnS_2 samples and electrodes were characterized by the scanning electron microscope (SEM, ZEISS). The ACTEM images are characterized by FEI Themis Z microscopes. The binding energies of the products of elements Sn, S before and after (de)sodiation reaction have been identified by X-ray photoelectron spectroscopy (XPS, Thermo-Fisher EscaLab 250Xi, Al Ka).

2.3. Cell assembly and electrochemical testing

The electrochemical performances of the SnS_2 electrodes were evaluated by employing CR2032 coin-type cells. The electrodes comprised the trigonal/hexagonal SnS_2, ketjen black and binder (CMC-Na) in a 7:2:1 wt ratio and dried in a vacuum oven at 65 °C for 5 h. The coin cells were assembled in an argon-filled glove-box with sodium metal as the counter electrodes and reference electrodes. 1 M $NaClO_4$ (PC: EC= 1:1 with 5% FEC by volume) was used as the electrolyte, and a glass fiber film served as a separator.

Galvanostatic charging and discharging measurements of the assembled cells were carried out at different current densities of the voltage range of 0.005 V–2.0 V versus Na^+/Na by using a Land (CT2001A, Wuhan) battery cycling machine. Cyclic voltammetry (CV) was executed by using a Solartron analytical electrochemical workstation at a scan rate of 0.1 mV s^{-1} between 0 and 2.5 V (vs. Na^+/Na) at

room temperature.

2.4. Nanobattery setup

The sodiation reaction was conducted inside TEM by the nanobattery setup on one homemade holder (Fig. S9), which is developed at the Center for X-Mechanics, Zhejiang University. It is composited by a compact four-degree freedom (positioning in X, Y, Z-directions plus self-rotation) nano-manipulator and *in situ* electrical biasing functions. Two kinds of SnS_2 nanoparticles were held with semicircular carbon film after shearing on one end of Au rod. Sodium metals were sketched by a tungsten probe and acted as the counter electrode in the Na ion batteries. The sodiation reaction occurs when a negative bias of ~2.5 V was applied between the two electrodes, and on the contrary, the desodiation reaction would be triggered once turn the bias to be positive. The whole morphology and microstructure evolutions were studied by *in situ* TEM mode and diffraction mode in real time with the dosage rate of ~100 e$^-$/(nm^2 S).

2.5. First-principles calculations

All the first-principles density functional theory (DFT) calculations were conducted using the Vienna Ab initio Simulation Package (VASP) [12–15] within the projector augmented wave (PAW) formalism [16] and the Perdew-Becke-Ernzerhof (PBE) approximation [17] was employed to deal with the exchange-correlation potential and vdW-D2 functional was adopted including a self-consistent van der Waals (vdW) correction [18]. Two different sets of parameters were used for configuration energy sampling and accurate total energy determination. For accurate total energy determination, a plane wave basis with a cut off energy of 520 eV and Γ-centered k-meshes with a density of 8000 k-points per reciprocal atom were used. For coarse energy sampling, energy cutoffs of 300 eV for the plane wave basis set was used with Γ-centered grids of approximately 4000 k-points per reciprocal atom.

2.6. Search for the non-equilibrium intercalation phases during sodiation

We used the Non-Equilibrium Phase Search (NEPS) method [19–21] to search for the non-equilibrium phases during the intercalation reaction process of SnS_2 by exploring geometrically distinct Na/Vacancy configurations on possible insertion sites of SnS_2 at different compositions (Na/vacancy ratios). It is assumed that during the non-equilibrium sodiation reaction, Na-ion diffusion is faster than Sn/S ions and therefore, Na-ion(s) can take any energetically favorable unoccupied sites while the migration/relocation of Sn/S ions is limited. The method then proceeded as follows: i) Identify all possible insertion sites in the SnS_2 structure using Materials Interface (MINT) [22]. We built a supercell containing 6 Sn^{4+} and S^{2-} ions with 12 empty sites in total. ii) All symmetrically different configurations were then generated using Enum [23,24] for a series of compositions $Na_x V_{3-x}SnS_2$ ($0 < x < 3$, V denotes vacancy). iii) Total energies of all configurations were sampled using settings described in the method section. iv) For each composition, corresponding structures were ranked by their total energies with the lowest three structures further relaxed in DFT with the accurate settings. We then calculated the formation energies of selected structures following reaction: $SnS_2 + xNa \rightarrow Na_xSnS_2$. v) Build the sodiation convex hull using the formation energies with the composition points on the hull were determined to be the non-equilibrium intermediate phases.

2.7. Voltage profile calculations

The average sodiation voltage (relative to Na/Na^+) can be computed using the negative of the reaction free energy per Na added/removed, as shown in Equation (1) [25]:

$$V = \frac{\Delta G_f}{F \Delta N_{Na}} \tag{1}$$

where F is the Faraday constant, ΔN_{Na} I s the amount of Na added/removed and ΔG_f is the (molar) change in free energy of the reaction. Considering a two-phase reaction between $Na_x SnS_2$ and $Na_y SnS_2$: $Na_x SnS_2 + (y - x) Na \rightarrow Na_y SnS_2$, ΔG_f can be approximated by the total internal energies from DFT calculations neglecting the entropic contributions (0 K),

$$\Delta E = E(Na_y SnS_2) - E(Na_x SnS_2) - (y - x)E(Na_{metal}) \tag{2}$$

where $E(Na_y SnS_2)$ and $E(Na_x SnS_2)$ are the DFT total energies at the respective compositions. The neglect of entropic contributions means that the lithiation voltage profiles will follow the T=0K ground state convex hull and consist of a series of constant voltage steps along the two-phase regions of the convex hull, separated by discontinuities which indicate the single phase compounds on the hull. It is worth mentioning here that, in practice, sodiation/desodiation do not necessarily proceed through two-phase reactions. Thus, the calculated T = 0 K voltage profiles should be viewed as an approximation to the actual voltage profiles [26]. The voltage drops in the profile become more rounded at finite temperatures (*e.g.*, room temperature) due to entropic effects [27].

3. Results and discussion

These two kinds of as-synthesized powders are identified by X-ray diffraction (XRD) pattern as trigonal SnS_2 phase (JCPDS No. 23–0677) with space group: $P\bar{3}m1$, lattice constants: $a = 3.645$ Å and $c = 5.8911$ Å (Fig. S1a); and hexagonal SnS_2 structure (JCPDS No. 89–3198), showing space group: $P6_3mc$, lattice constants: $a = 3.645$ Å and $c = 11.802$ Å

(Fig. S1c). Meanwhile, the XRD patterns indicate the high purity and well crystallization of both the two kinds of SnS_2 powders.

The atomic arrangements of Sn and S in both trigonal and hexagonal SnS_2 along [001] and $[\bar{1}\bar{1}0]$ axis zone are representatively revealed by scanning TEM high-angle annular dark-field (STEM-HAADF) observations (Fig. 1a-b and e-f), respectively. In Fig. 1a, the brighter atoms are determined to be Sn atoms due to their larger atomic number compared to that of S [28], while the brighter atoms belong to Sn-S atom groups in Fig. 1e. According to Fig. 1b and f, the sandwich-like Sn-S group corresponds to a well-defined layered structure along [001] directions, providing open channels to facilitate fast alkali ion intercalation and diffusion. As shown in Fig. 1c and Fig. S1b, the trigonal SnS_2 plates have the width of 400–600 nm and thickness around 50 nm, which is somewhat smaller than that of hexagonal SnS_2 plates in Fig. 1g and Fig. S1d. One individual plate has an excellent single crystal structure revealed clearly by the inset SAED pattern taken from [001] zone axis of both trigonal and hexagonal phases, as shown in Fig. 1c and Fig. 1g. Trigonal SnS_2 is 2H polytype due to two sulfur layers in one unit cell [29], and the structural symmetry of S and Sn atom layers is $[(cBa)]_n$ when viewed along $[\bar{1}\bar{1}0]$ direction (see Fig. 1d), where Sn atom layer (labeled with B) locates at bilevel S atom layers (labeled with c and a). However, 4H polytype of hexagonal SnS_2 has four sulfur layers in one unit cell, S and Sn atom layers are stacking with the order of $[(bCa)(cBa)]_n$, where two Sn atom layers (C and B) are situated between the two nearest-neighbor S atom layers (b and a, c and a), respectively. Even though the interlayer distances are same for the 2H and 4H SnS_2 [30], the structural symmetry difference in the polytype periodicity will directly affect the physical and chemical properties of materials like variation of the bandgap [31]. Alkali ions can intercalate into the octahedral and tetrahedral sites of S-S interlayers in 2D layer SnS_2 in sequence, because the octahedral sites have the lowest energy for ions intercalation [9,32].
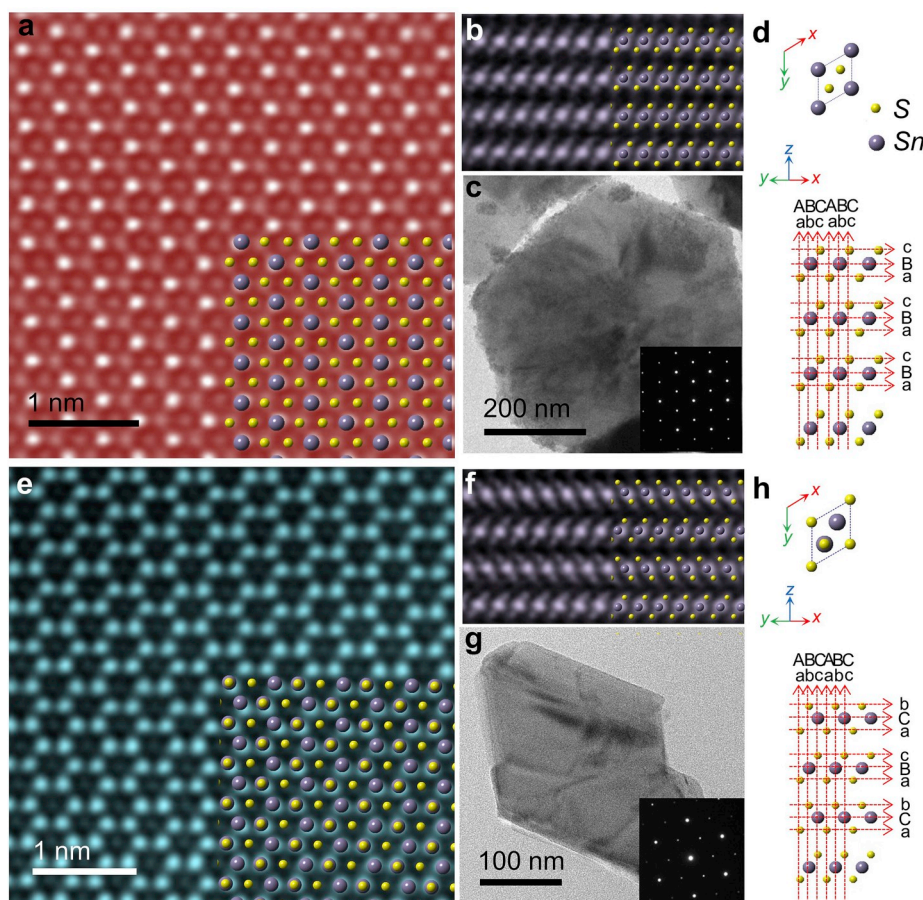

Fig. 1. Characterization of SnS_2 nanoplate with different structural symmetry. The structural and morphological image of trigonal (a–d) and hexagonal (e–h) SnS_2 nanoplate. (a) and (e) are the atomic scale ACTEM images are observed along [001] direction, (b) and (f) are along $[\bar{1}\bar{1}0]$ direction. (c) and (g) are the typical TEM topographies of an individual trigonal and hexagonal SnS_2 nanoplate, respectively, the insets in (c) and (g) are the corresponding selected area electron diffraction (SAED) pattern viewed along zone axis [001]. The Atomic model of the 2H trigonal $P\bar{3}m1$ SnS_2 in (d) and 4H hexagonal $P6_3mc$ SnS_2 in (h), showing a $[(cBa)]_n$ and $[(bCa)(cBa)]_n$ structural symmetry of S and Sn atom layers, respectively.

Density functional theory (DFT) calculation predicts the formation of possible intermediate phases of trigonal and hexagonal SnS_2 in Na insertion processes, as shown in Fig. 2. It is generally believed that the sodiation of 2D metal sulfides will start from the intercalation of Na ions into the S-S interlayers bonded by the weak van der Waals force [33]. Three intermediate phases may form during first sodiation of trigonal $P\bar{3}m1$ SnS_2, which are denoted as AA1 ($NaSnS_2$), AA2 ($NaSnS_2$) and AA3 ($NaSnS_2$). Hereinto, AA1 structure has the lowest relative energy and is the most stable (Fig. 2). As to hexagonal $P6_3mc$ SnS_2, AB1 ($NaSnS_2$) is much more stable than AB2 ($NaSnS_2$). For both AA1 and AB1 $NaSnS_2$, all sodium ions are inserted into octahedral sites of two different SnS_2 unit cells. The main difference between these two structures are the stacking sequence of S, Sn and Na atoms in their corresponding unit cell. For AA1 $NaSnS_2$, Na ions are respectively inserted into one quarter and three quarters height of the four edges along c axis, the atomic stacking sequence is Sn-S-Na from the side-view direction. From top-view direction, Na atoms are lined in one column with Sn atoms, two column of S atoms are respectively located at one quarter and three quarters of the crosscourt direction of two Sn atoms with acute angle. Whereas for AB1 $NaSnS_2$, Na ions are intercalated into the unit cell body with stacking sequence of S-Sn-S-Na along side-view direction. From top-view direction observation, sodium ions are located at one quarter (Sn-Na-S column) and three quarters (S-Sn-Na column) of the crosscourt direction of two S atoms with acute angle under different depth, respectively.
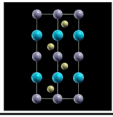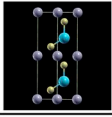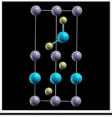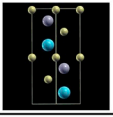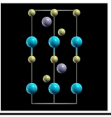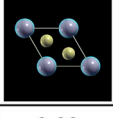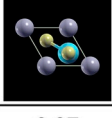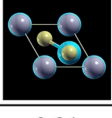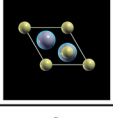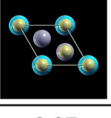
Fig. 3 and Movie S1a show the real-time microstructure evolutions of SnS_2 in Na insertion through *in situ* selected area electron diffraction (SAED), which are collected at a low electron beam dose to reduce the radiation damage to the sample [33]. As indicated in Fig. 3a, the real-time SAED pattern reveals d-spacing of 3.135 Å and 1.810 Å belong to the $(\bar{1}00)$ and (110) of pristine trigonal SnS_2, respectively. As Na ion insertion, the lattice spacing keeps constantly enlarging. That means the formation of semi-stable intermediate phases before initially trigonal/hexagonal SnS_2 phase completely transforms to AA1/AB1 $NaSnS_2$. They are separately denoted as Na_xSnS_2 ($0<x<1$) and Na_ySnS_2 ($0<y<1$). After reacting to 1min 21s, the diffraction spot (110) splits to two weak spots, as shown in the inset picture of Fig. 3b, indicating a characteristic of the two-phase coexistence. They can be ascribed to the SnS_2's d_{110} (1.803 Å) and Na_xSnS_2's d_{110} (1.922 Å), respectively. When the reaction proceeds to 2 min, the spot with the spacing of 1.803 Å disappeared and the spacing of remained spot can be calculated to 1.947 Å (Fig. 3c). With sodium further intercalation to 2min 27s, the diffraction spot of $(\bar{1}00)$ splits to two spots with respective d-spacing of 3.309 Å and 3.328 Å, and the (110) d-spacing are enlarged to 1.973 Å. Moreover, these three diffraction spots keep moving close toward (000) (Fig. 3d), meaning that the value of x in the corresponding Na_xSnS_2 phase keeps increasing. Finally, after 2min 34s, the spacings of diffraction spots of $(\bar{1}00)$ and (110) extend to 3.367 Å and 1.985 Å, and the AA1 $NaSnS_2$ (x=1) phase is

entirely formed with theoretical volume expansion of 42.27%.

Supplementary video related to this article can be found at https ://doi.org/10.1016/j.nanoen.2019.104276.

Similarly, Fig. 3f–j and Movie S1b demonstrate real-time SAED evolution of hexagonal SnS_2. Fig. 3f shows the [001] SAED pattern of pristine hexagonal SnS_2. When Na ion intercalation lasts for 6s, the (110) diffraction spot splits to two corresponding to SnS_2's d_{110} (1.843 Å) and Na_ySnS_2's d_{110} (1.896 Å), respectively. After 3min 59s, the d_{110} of Na_ySnS_2 enlarges to 1.850 Å and 1.942 Å (Fig. 3h). As the intercalation reaction carries out for 5min 30s, one spot totally disappears and the spacing of remaining spot increase to 1.954 Å (Fig. 3i), accompanying with the value of y in Na_ySnS_2 further magnifying. Finally, after 6min 38s (Fig. 3j), the d-spacings of (110) and $(\bar{1}00)$ increase to 1.983 Å and 3.328 Å respectively, which can be indexed to hexagonal AB1 $NaSnS_2$ phase with theoretical volume expansion of 42.27%. Slightly moving closer to {000} of all of the diffraction spots in Fig. 3, mainly results from the expansion of the unit cell (trigonal SnS_2: 10.33% for a axis, and 18.6% for c axis; hexagonal SnS_2: 10.29% for a axis, 16.96% for c axis). The initial phase transits from layered SnS_2 to AA1 or AB1 $NaSnS_2$. Besides, the theoretical calculation results further prove that the electrochemical sodiation starts from Na ions successively taking up octahedral and tetrahedral sites between two single SnS_2 layers in both trigonal and hexagonal SnS_2 phases (Fig. S2).

When the intercalation number of Na ions archive to the critical value, SnS_2 single crystal is generally rearranged and then finally collapsed, indicated by the disappearance of the ordered diffraction spots and appearance of the broad diffraction rings. That stands for the happening of the following conversion and alloying reactions upon further sodiation. The yellow arrows in Fig. 4 represent the sodiation processes, while the blue arrows represent the desodiation processes. The diffused diffraction rings appeared outside of $\{\bar{1}00\}$ can be indexed to SnS (Orthorhombic, Pbnm, JCPDS No. 39–0354), and it shows up in both trigonal and hexagonal SnS_2 (Fig. 4, Stage I; Movie S1a, b). With the vanishing of the single crystal matrix, the diffraction ring become β-Sn polycrystals and gets clearer and sharper, implying the β-Sn phase gradually grows up (Fig. 4, Stage II), the amorphous Na_2S may form in the meantime [34]. Continually reacting with Na ions, amorphous $Na_{15}Sn_4$ (green ring) and polycrystal Na_2S (yellow ring) are forming with the occurrence of the blur diffraction rings (Fig. 4, Stage III), as seen in Movie S2. This kind of phase transformation is similar to the previous reports [35,36]. And further proved with identifying $Na_{15}Sn_4$ by the ex-situ XRD characterization in half-cell testing in our experiments, as shown in Fig. S3. However, due to the incomplete reaction of the electrode materials, some metallic β-Sn phases remain after discharge to 0.005 V in the half-cell testing. When an opposite voltage is applied, the broaden diffraction ring is successively replaced by sharper ones, implying that $Na_{15}Sn_4$ are gradually dealloyed to Na metal and SnS

SnS_2	Trigonal			Hexagonal	
Models	AA1	AA2	AA3	AB1	AB2
[110]					
[001]					
Relative Energy (eV)	0.09	0.37	0.21	0	0.37

● Na
● Sn
● S

Fig. 2. DFT-calculated prediction atomic models of Na insertion intermediate phases of trigonal and hexagonal SnS_2 and the corresponding energies of different simulated phases.
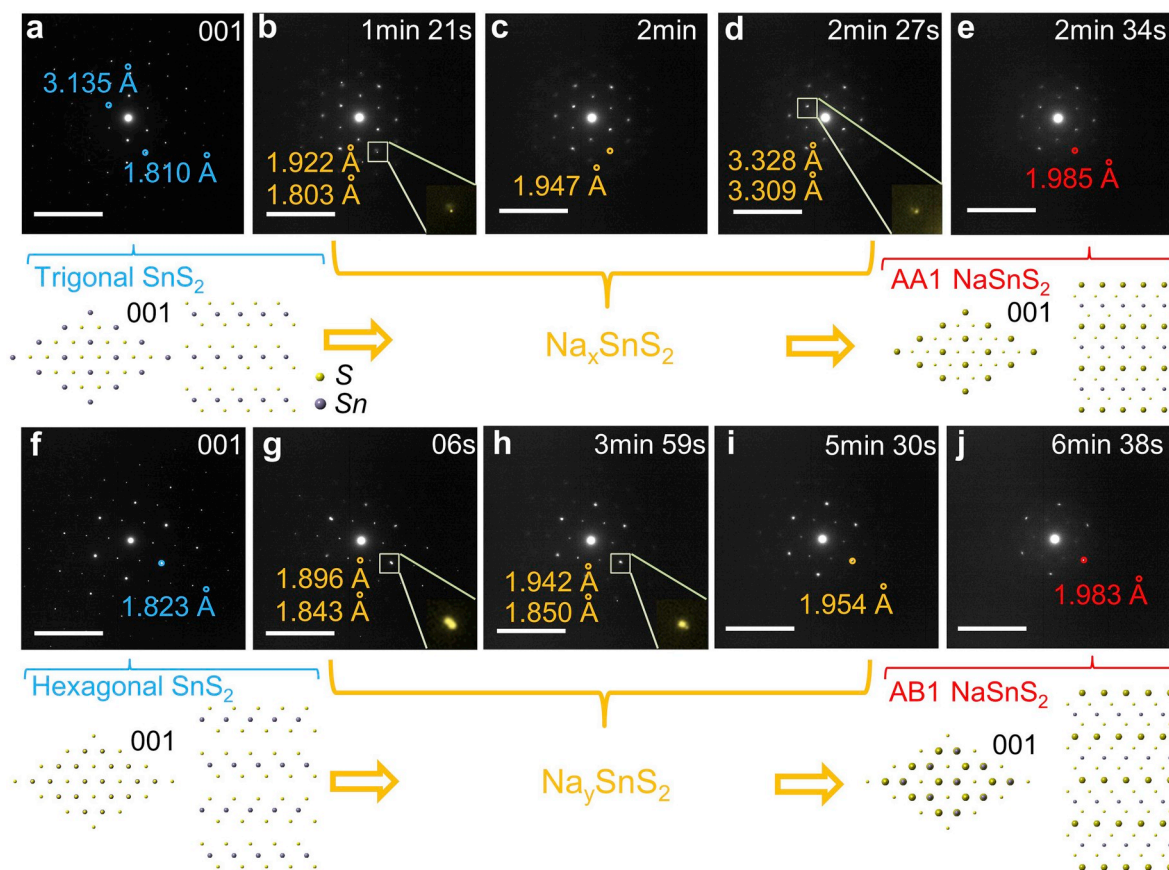
Fig. 3. Real-time SAED patterns of trigonal (a–e) and hexagonal SnS$_2$ (f–j) individual nanoplate upon Na insertion.
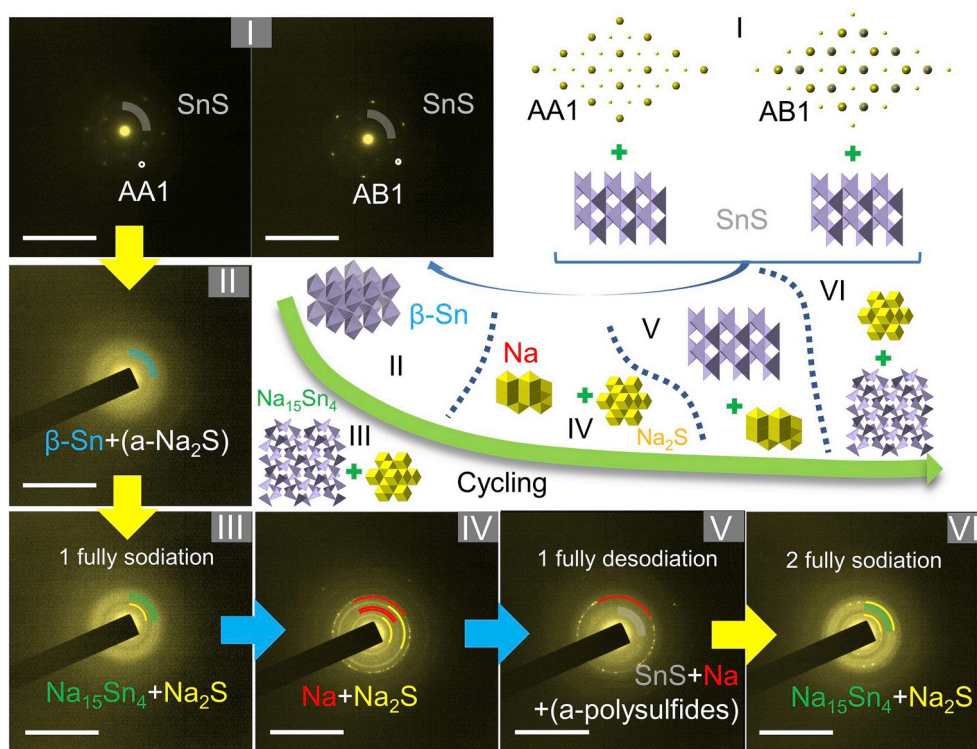

Fig. 4. Real-time SAED patterns of trigonal and hexagonal SnS$_2$ individual nanoplate upon Na insertion in conversion-alloying reaction. The yellow arrows represent sodium ion insertion and the blue arrows indicate sodium ion extraction.

phase. The early report showed that controllable removal of chalcogen atoms due to electron irradiation may cause rhombohedral layered SnS_2 transform into highly anisotropic orthorhombic layered SnS [37], so XPS and XRD are used here in addition to identify the chemical state of Sn and S in Stage V, indicating the existence of Sn^{2+} and S^{2-} (Fig. 5, Fig. S4 and Fig. S10). Thus the final phase after desodiation can be ascribed to SnS. Moreover, Na_2S phase vanishes and may transform to amorphous polysulfides (a-polysulfides) [38], as shown in Stage IV - V of Fig. 4 and Movie S3. In the following cycles, the reversible alloying reaction is taken place between SnS and $Na_{15}Sn_4$ phase (Fig. 4, Stage VI and Movie S4). Generally, the conversion reaction between Na_xSnS_2 and Sn, Na_2S phase is considered to be irreversible [39,40]. However, the Na_2S phase is reversibly transformed to polysulfides (Na_2S_m, $2<m<8$) in desodiation. This may originate from better reaction kinetics with short diffusion distance owing to individual nanoparticle testing. Similar phenomenon has been found in other kinds of metal sulfides, such as CuS [41] and MoS_2 [42] electrodes.

Supplementary video related to this article can be found at https://doi.org/10.1016/j.nanoen.2019.104276.

Na-ion diffusion difference has been studied by monitoring the axis change along [001] and [100] directions, revealing anisotropic volume expansion in both trigonal and hexagonal SnS_2 phases during sodiation process. As shown in Fig. S5, the dimensional increment along [001] direction is almost four times larger than that of [100] direction due to the diffusion path preference and insertion in S-S interlayers of Na ions in 2D materials [43]. It is worthy of mentioning that hexagonal SnS_2 plates can't shrink to the original size after full desodiation (Fig. S6). The spacing of lattice plane vertical to incident beam ([001] direction), is identified as 4.19% larger than that in full sodiation states. That means the closed-packed single-crystal is dramatically loosened by many defects forming and involvement in the (de)sodiation reaction.

Fig. 5a shows of CVs of trigonal/hexagonal SnS_2 electrodes of half-cell examined from 0 to 2.5 V at a scanning rate of $0.1\,mV\,s^{-1}$. Three visibly reduction peaks exist in the first cathodic process, *i.e.* 1.7 V, 1.1 V, and the range from 0.3 V to 0.7 V. They are respectively related to the Na-ion intercalation, the formation of solid electrolyte interphase (SEI) layer, and the synergetic conversion and alloying reactions [44, 45]. Meantime, three corresponding oxidation peaks appear at around of 0.3 V, 0.7 V, and 1.2 V, corresponding to the desodiation of Na-Sn and Na-S phases; reformation of SnS nanoparticles and polysulfides. All the reaction steps have also been identified in the charge/discharge voltage

plateaus in Fig. S7.

To confirm the chemical state of S in the (de)sodiation process, X-ray photoelectron spectroscopy (XPS) has been used to investigate the valence changes of sulfur at different states in cycles, as shown in Fig. 5b. The binding energy (BE) of S 2p doublets in SnS_2 electrode of open-circuit voltage (OCV) is found to be $161.9 \pm 0.1\,eV$ (S $2p_{3/2}$) and 163.3 (S $2p_{1/2}$) in agreement with the former study [46,47]. When it is reduced, the main peak position shifts as expected from S^{2-} to lower oxidation states to lower BE [48,49]. After discharging to 0.005 V, a shift in the sulfur peak is observed to 160.16 (S $2p_{3/2}$) and 161.23 eV (S $2p_{1/2}$), which can be ascribed to the formation of Na_2S [50–52]. And the conversion reaction leads to the broadening of the peaks, the region within the binding energy between Na_2S and elemental sulfur is most reasonably assigned to the sodium polysulfides Na_2S_m ($2<m<8$) [49]. When the electrode is charged to 2.5 V, one dual peak at 161.0 eV and 162.4 eV corresponds to S $2p_{3/2}$ and S $2p_{1/2}$ of SnS [53], respectively. The other dual peaks have higher BE of 161.8 eV and 163.1 eV, which means the formation of polysulfides $[S_m]^{2-}$ [54].

Based on the analysis for the discharge/charge process above, the chemical reactions to electrochemical cycles can be written as below,

$$SnS_2 + Na \rightarrow NaSnS_2 \tag{3}$$

$$NaSnS_2 \rightarrow SnS + Na_2S \tag{4}$$

$$SnS + 2Na \leftrightarrow \beta\text{-}Sn + Na_2S \tag{5}$$

$$4\beta\text{-}Sn + 15Na \leftrightarrow Na_{15}Sn_4 \tag{6}$$

$$Na_2S \leftrightarrow Na_2S_m \ (2<m<8) \tag{7}$$

To investigate the phase transformation of SnS_2, density functional theory (DFT) calculations are introduced to calculate the computional formation energy of all compounds in a ternary Na-Sn-S ground state convex hull. All compounds within the Na-Sn-S phase space were adopted from the Inorganic Crystal Structure Database (ICSD) [55]. Fig. 6a shows the Na-Sn-S phase diagram (0 K) which is constructed by calculations within the Open Quantum Materials Database (OQMD) framework [56]. All thermodynamically stable compounds are marked on the phase diagram. The tie-line between SnS_2 and Na, which goes through various intermediate phases and multi-phase zones, is the equilibrium sodiation reaction pathway of SnS_2. These intermediate phases correspond to various sodiation reactions as listed in Table S1, where the voltages and capacities are calculated as well.

Fig. 6c shows calculated equilibrium voltage profile has a great agreement with the experimental curves at high Na-content ($4 < x < 31/4$) which corresponds to the alloying reactions. However, the initial sodiation voltage segment exhibits large difference with the experimental counterpart. Non-equilibrium sodiation process of ground state SnS_2 (trigonal) has been involved to ulteriorly fit the results by using an in-house code described in the method section. Elemental reference states (Na, Sn, S) were obtained by fitting to experimental formation energies, from the SGTE substance database (SSUB) and a database constructed by P. Nash et al. [57–60]. Two kinds of intermediate intercalation phases, *i.e.* Na_xSnS_2 with x of 0.25, and 1, are identified as shown in Fig. 6b. Initially ($x = 0.25$), Na-ions are predicted to occupy the O_h empty sites and the system reaches the $NaSnS_2$ phase when all the O_h sites are taken (Fig. 6c). Na-ions then start to occupy the empty T_d sites and the system begins to lose structural stability, triggering the subsequent conversion reactions. At $x = 2$, the system is predicted to be phase separated to SnS and Na_2S. Calculated non-equilibrium voltage profile ($0 < x < 2$) shows great agreement with the experimental curve as shown in Fig. 6c and Fig. S8. Since the non-equilibrium intercalation sodiation lowers the voltage level, the following conversion stage ($2 < x < 4$) also occurs at a lowered voltage, which also agrees with the experimental plateau (Fig. 6c). After all the Sn-ions being reduced to their metallic states, the sodiation proceeds in the alloying manner with stable intermediate phases including $NaSn_2$, NaSn, Na_9Sn_4, $Na_{15}Sn_4$, and
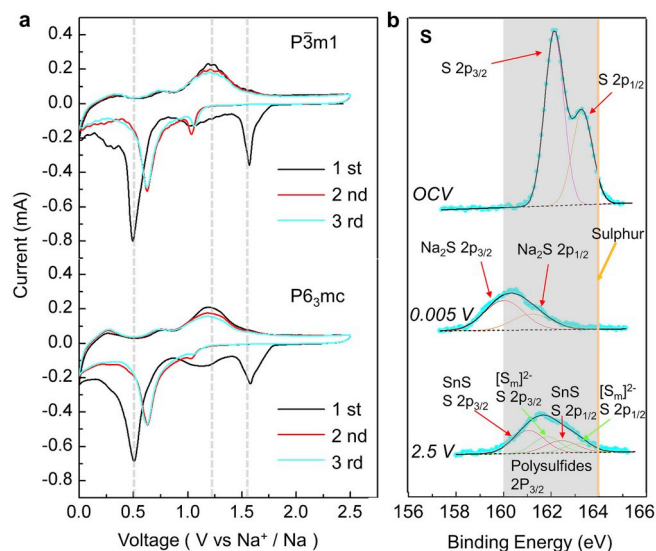

Fig. 5. (a) CVs of the first three cycles of electrodes using trigonal/hexagonal SnS_2 as active materials; (b) XPS spectra for S 2p levels of hexagonal SnS_2 at open circuit voltage, first sodiation to 0.005 V, and first desodiation to 2.5 V.
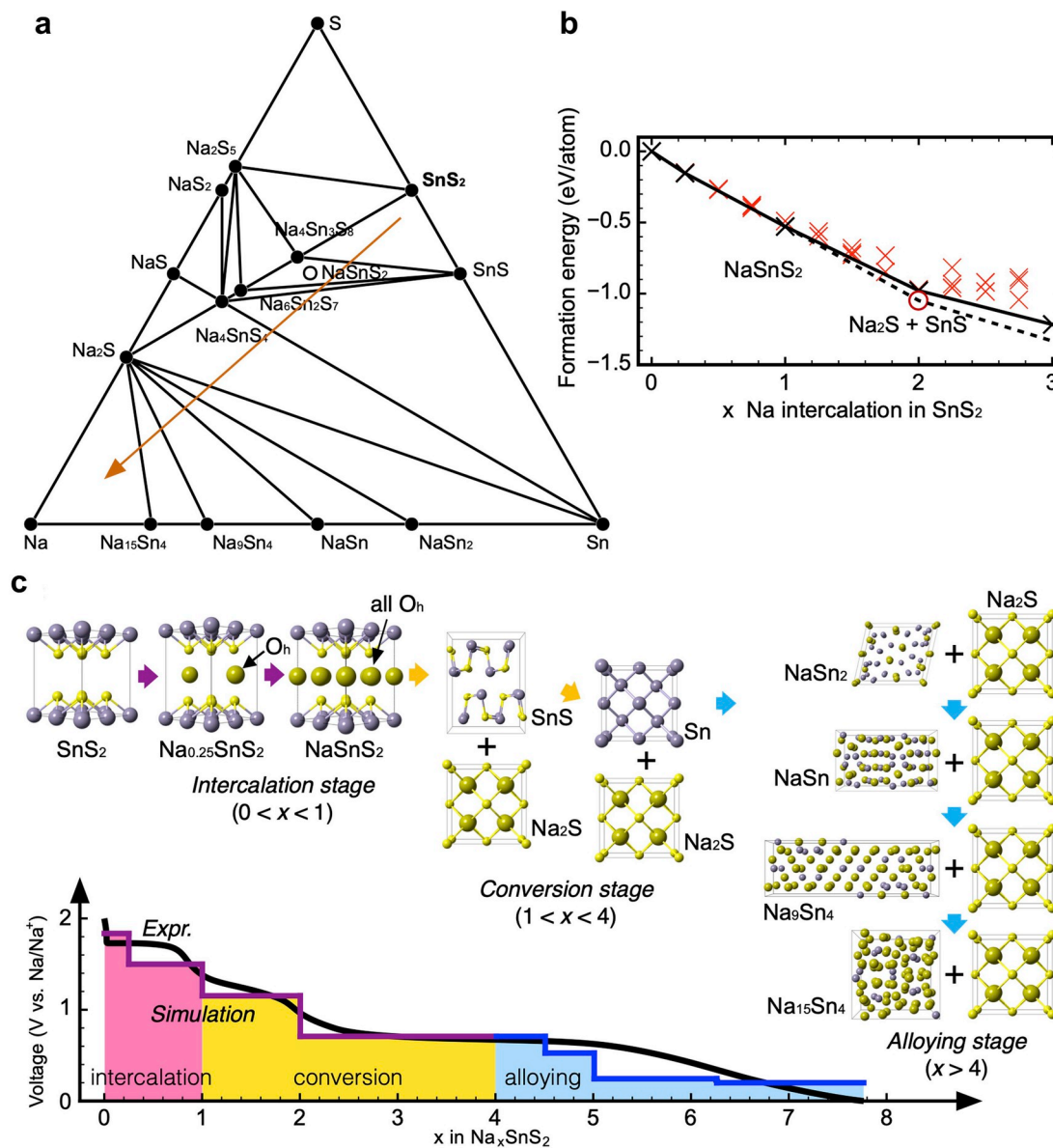
Fig. 6. Electrochemical sodiation process of SnS_2. (a) Na-Sn-S phase diagram (0 K). (b) Non-equilibrium intercalation sodiation convex hull of SnS_2. (c) Structural evolution during the whole sodiation process of SnS_2 which proceed in three stages: intercalation → conversion → alloying and the predicted voltage profile from DFT which shows great agreement with the experiment voltage curve.

the voltage profile keep decreasing as observed in the experiment (Fig. 6c).

4. Conclusions

A comparative mechanistic study and reaction dynamics research of two kinds of SnS_2 with different structural symmetry, *i.e.* trigonal ($P\bar{3}m1$) and hexagonal ($P6_3mc$), have been deeply conducted in the (de) sodiation processes by the combing techniques of *in situ* TEM, *ex situ* XPS and the first-principles calculations. Upon Na ion insertion, two-phase coexistence phenomenon is observed in both trigonal and hexagonal SnS_2. When all the O_h sites are occupied by Na-ions, stable intermediate phase of AA1 $NaSnS_2$ is formed based on the trigonal SnS_2 and, however, AB1 $NaSnS_2$ shows up based on the hexagonal SnS_2 matrix. Na ions tend to insert into the S-S layers along [001] direction, leading to much larger increment along [001] than other directions. After the empty T_d sites are taken up by Na ions, the system begins to lose structural stability, triggering the subsequent conversion and alloying reactions. The

intercalation phases of AA1/AB1 $NaSnS_2$ sequentially transit to SnS/ β-Sn and Na_2S, then to $Na_{15}Sn_4$ and Na_2S upon full sodiation. On the contrary, they return to SnS and Na_2S_m (2<m<8) phases when Na ions complete extraction. Our findings lead to a mechanistic understanding of nanoscale (de)sodiation behavior of SnS_2 with different structures and may provide valuable implications to other 2D metal chalcogenides.

Author contributions

A.N., H.W. and Q.L. initiated the project and created the experimental protocols. Z. M. and Q.L. conducted the *in-situ* TEM testing and corresponding data analysis. B.G. and C.L. carried out the battery testing of SnS_2. Z.Y., Y.C., and X.Z., and A. A.-G. performed the DFT calculations. Z.M., Q.L., H.W. and A. N. wrote the manuscript and all the authors contributed to the discussion and revision of the manuscript.

Declaration of competing interest

The authors declare that they have no known competing financial interests or personal relationships that could have appeared to influence the work reported in this paper.

Acknowledgements

Appendix A. Supplementary data

Supplementary data to this article can be found online at https://doi.org/10.1016/j.nanoen.2019.104276.

References

[1] S. Komaba, W. Murata, T. Ishikawa, N. Yabuuchi, T. Ozeki, T. Nakayama, A. Ogata, K. Gotoh, K. Fujiwara, Electrochemical Na insertion and solid electrolyte interphase for hard-carbon electrodes and application to Na-ion batteries, Adv. Funct. Mater. 21 (2011) 3859–3867. https://onlinelibrary.wiley.com/doi/full/10.1002/adfm.201100854.

[2] D. Larcher, J.-M. Tarascon, Towards greener and more sustainable batteries for electrical energy storage, Nat. Chem. 7 (2015) 19. https://www.nature.com/articles/nchem.2085.

[3] Y. Liu, X.-Y. Yu, Y. Fang, X. Zhu, J. Bao, X. Zhou, X.W.D. Lou, Confining SnS_2 ultrathin nanosheets in hollow carbon nanostructures for efficient capacitive sodium storage, Joule 2 (2018) 725–735. https://www.sciencedirect.com/science/article/pii/S2542435118300047.

[4] C. Ma, J. Xu, J. Alvarado, B. Qu, J. Somerville, J.Y. Lee, Y.S. Meng, Investigating the energy storage mechanism of SnS2-rGO composite anode for advanced Na-ion batteries, Chem. Mater. 27 (2015) 5633–5640.

[5] Q. Huang, L. Wang, Z. Xu, W. Wang, X. Bai, In-situ TEM investigation of MoS_2 upon alkali metal intercalation, Sci. China Chem. 61 (2018) 222–227. https://link.springer.gg363.site/article/10.1007/s11426-017-9128-0.

[6] Z. Ma, Y. Lyu, H. Yang, Q. Li, B. Guo, A. Nie, Systematic investigation of the Binder's role in the electrochemical performance of tin sulfide electrodes in SIBs, J. Power Sources 401 (2018) 195–203. https://www.sciencedirect.com/science/article/pii/S0378775318309492.

[7] B. Pałosz, S. Gierlotka, W. Pałosz, Polytypism of SnS_2 crystals grown by chemical transport; effect of growth conditions on the structure of polytypes, Bull. Mineral. 109 (1986) 143–150. https://www.persee.fr/doc/bulmi_0180-9210_1986_act_109_1_7923.

[8] P. Gao, Y.-Y. Zhang, L. Wang, S. Chen, Y. Huang, X. Ma, K. Liu, D. Yu, In situ atomic-scale observation of reversible sodium ions migration in layered metal dichalcogenide SnS_2 nanostructures, Nano Energy 32 (2017) 302–309. https://www.sciencedirect.com/science/article/pii/S2211285516306176.

[9] S. Hwang, Z. Yao, L. Zhang, M. Fu, K. He, L. Mai, C. Wolverton, D. Su, Multistep lithiation of tin sulfide: an investigation using in situ electron microscopy, ACS Nano 12 (2018) 3638–3645. https://pubs.acs.org/doi/abs/10.1021/acsnano.8b00758.

[10] K. Yin, M. Zhang, Z.D. Hood, J. Pan, Y.S. Meng, M. Chi, Self-assembled framework formed during lithiation of SnS_2 nanoplates revealed by in situ electron microscopy, Accounts Chem. Res. 50 (2017) 1513–1520. https://pubs.acs.org/doi/abs/10.1021/acs.accounts.7b00086.

[11] G. Kresse, J. Hafner, Ab initio molecular dynamics for liquid metals, Phys. Rev. B 47 (1993) 558–561. https://link.aps.org/doi/10.1103/PhysRevB.47.558.

[12] G. Kresse, J. Hafner, Ab initio molecular-dynamics simulation of the liquid-metal-amorphous-semiconductor transition in germanium, Phys. Rev. B 49 (1994) 14251–14269. https://link.aps.org/doi/10.1103/PhysRevB.49.14251.

[13] G. Kresse, J. Furthmüller, Efficiency of ab-initio total energy calculations for metals and semiconductors using a plane-wave basis set, Comput. Mater. Sci. 6 (1996) 15–50. http://www.sciencedirect.com/science/article/pii/0927025696000080.

[14] G. Kresse, J. Furthmüller, Efficient iterative schemes for ab initio total-energy calculations using a plane-wave basis set, Phys. Rev. B 54 (1996) 11169–11186. https://link.aps.org/doi/10.1103/PhysRevB.54.11169.

[15] P.E. Blöchl, Projector augmented-wave method, Phys. Rev. B 50 (1994) 17953–17979. https://link.aps.org/doi/10.1103/PhysRevB.50.17953.

[16] J.P. Perdew, M. Ernzerhof, K. Burke, Rationale for mixing exact exchange with density functional approximations, J. Chem. Phys. 105 (1996) 9982–9985. https://doi.org/10.1063/1.472933.

[17] H. Peelaers, C.G. Van de Walle, First-principles study of van der Waals interactions in MoS_2 and MoO_3, J. Phys. Condes. Mater. 26 (2014) 305502, https://doi.org/10.1088/0953-8984/26/30/305502.

[18] Z. Yao, S. Kim, J. He, V.I. Hegde, C. Wolverton, Interplay of cation and anion redox in $Li_4Mn_2O_5$ cathode material and prediction of improved $Li_4(Mn,M)_2O_5$ electrodes for Li-ion batteries, Sci. Adv. 4 (2018), eaao6754. https://advances.sciencemag.org/content/advances/4/5/eaao6754.full.pdf.

[19] C. Zhan, Z. Yao, J. Lu, L. Ma, V.A. Maroni, L. Li, E. Lee, E.E. Alp, T. Wu, J. Wen, Y. Ren, C. Johnson, M.M. Thackeray, M.K.Y. Chan, C. Wolverton, K. Amine, Enabling the high capacity of lithium-rich anti-fluorite lithium iron oxide by simultaneous anionic and cationic redox, Nat. Energy 2 (2017) 963–971, https://doi.org/10.1038/s41560-017-0043-6.

[20] Z. Yao, S. Kim, M. Aykol, Q. Li, J. Wu, J. He, C. Wolverton, Revealing the conversion mechanism of transition metal oxide electrodes during lithiation from first-principles, Chem. Mater. 29 (2017) 9011–9022, https://doi.org/10.1021/acs.chemmater.7b02058.

[21] L. Ward, K. Michel, Materials/Mint: Initial Release, 2016, https://doi.org/10.5281/zenodo.167890.

[22] G.L.W. Hart, L.J. Nelson, R.W. Forcade, Generating derivative structures at a fixed concentration, Comput. Mater. Sci. 59 (2012) 101–107. http://www.sciencedirect.com/science/article/pii/S092702561200081X.

[23] G.L.W. Hart, R.W. Forcade, Algorithm for generating derivative structures, Phys. Rev. B 77 (2008) 224115. https://link.aps.org/doi/10.1103/PhysRevB.77.224115.

[24] M.K. Aydinol, A.F. Kohan, G. Ceder, K. Cho, J. Joannopoulos, Ab initio study of lithium intercalation in metal oxides and metal dichalcogenides, Phys. Rev. B 56 (1997) 1354–1365. https://link.aps.org/doi/10.1103/PhysRevB.56.1354.

[25] M.K.Y. Chan, C. Wolverton, J.P. Greeley, First principles simulations of the electrochemical lithiation and delithiation of faceted crystalline silicon, J. Am. Chem. Soc. 134 (2012) 14362–14374, https://doi.org/10.1021/ja301766z.

[26] C. Wolverton, A. Zunger, First-principles prediction of vacancy order-disorder and intercalation battery voltages in Li_xCoO_2, Phys. Rev. Lett. 81 (1998) 606–609. https://link.aps.org/doi/10.1103/PhysRevLett.81.606.

[27] D. Garcia-Gutierrez, C. Gutierrez-Wing, M. Miki-Yoshida, M. Jose-Yacaman, HAADF study of Au-Pt core-shell bimetallic nanoparticles, Appl. Phys. A 79 (2004) 481–487, https://doi.org/10.1007/s00339-004-2600-7.

[28] R.S. Mitchell, Y. Fujiki, Y. Ishizawa, Structural polytypism of SnS_2, Nature 247 (1974) 537–538, https://doi.org/10.1038/247537a0.

[29] B. Palosz, W. Steurer, H. Schulz, Refinement of SnS_2 polytypes 2H, 4H and 18R, Acta Crystallogr. B 46 (1990) 449–455, https://doi.org/10.1107/S0108768189012577.

[30] S. Acharya, O.N. Srivastava, Electronic bandgap measurements of SnS_2 polytypes, Phys. Status Solidi A 56 (1979) K1–K4. https://onlinelibrary.wiley.com/doi/abs/10.1002/pssa.2210560147.

[31] I. Lefebvre-Devos, J. Olivier-Fourcade, J.C. Jumas, P. Lavela, Lithium insertion mechanism in SnS_2, Phys. Rev. B 61 (2000) 3110–3116. https://journals.aps.org/prb/abstract/10.1103/PhysRevB.61.3110.

[32] Q. Li, Y. Xu, Z. Yao, J. Kang, X. Liu, C. Wolverton, M.C. Hersam, J. Wu, V.P. Dravid, Revealing the effects of electrode crystallographic orientation on battery electrochemistry via the anisotropic lithiation and sodiation of ReS_2, ACS Nano 12 (2018) 7875–7882, https://doi.org/10.1021/acsnano.8b02203.

[33] Q. Li, Z. Yao, J. Wu, S. Mitra, S. Hao, T.S. Sahu, Y. Li, C. Wolverton, V. Dravid, Intermediate phases in sodium intercalation into MoS_2 nanosheets and their implications for sodium-ion batteries, Nano Energy 38 (2017) 342–349. https://www.sciencedirect.com/science/article/pii/S2211285517303439.

[34] A. Kitajou, J. Yamaguchi, S. Hara, S. Okada, Discharge/charge reaction mechanism of a pyrite-type FeS2 cathode for sodium secondary batteries, J. Power Sources 247 (2014) 391–395. http://www.sciencedirect.com/science/article/pii/S0378775313014730.

[35] S. Komaba, Y. Matsuura, T. Ishikawa, N. Yabuuchi, W. Murata, S. Kuze, Redox reaction of Sn-polyacrylate electrodes in aprotic Na cell, Electrochem. Commun. 21 (2012) 65–68. https://www.sciencedirect.com/science/article/pii/S1388248112002111.

[36] Y. Zhang, P. Zhu, L. Huang, J. Xie, S. Zhang, G. Cao, X. Zhao, Few-layered SnS_2 on few-layered reduced graphene oxide as Na-ion battery anode with ultralong cycle life and superior rate capability, Adv. Funct. Mater. 25 (2015) 481–489. https://onlinelibrary.wiley.gg363.site/doi/abs/10.1002/adfm.201402833.

[37] E. Sutter, Y. Huang, H.P. Komsa, M. Ghorbani-Asl, A.V. Krasheninnikov, P. Sutter, Electron-beam induced transformations of layered tin dichalcogenides, Nano Lett. 16 (2016) 4410–4416, https://doi.org/10.1021/acs.nanolett.6b01541.

[38] Z. Hu, Q. Liu, S.-L. Chou, S.-X. Dou, Advances and challenges in metal sulfides/selenides for next-generation rechargeable sodium-ion batteries, Adv. Mater. 29 (2017) 1700606, https://doi.org/10.1002/adma.201700606.

[39] Y. Zhang, P. Zhu, L. Huang, J. Xie, S. Zhang, G. Cao, X. Zhao, Few-layered SnS_2 on few-layered reduced graphene oxide as Na-ion battery anode with ultralong cycle life and superior rate capability, Adv. Funct. Mater. 25 (2015) 481–489. https://onlinelibrary.wiley.com/doi/abs/10.1002/adfm.201402833.

[40] B. Qu, C. Ma, G. Ji, C. Xu, J. Xu, Y.S. Meng, T. Wang, J.Y. Lee, Layered SnS_2-reduced graphene oxide composite-A high-capacity, high-rate, and long-cycle life

sodium-ion battery anode material, Adv. Mater. 26 (2014) 3854–3859. https://onlinelibrary.wiley.com/doi/abs/10.1002/adma.201306314.

[41] J.Y. Park, S.J. Kim, J.H. Chang, H.K. Seo, J.Y. Lee, J.M. Yuk, Atomic visualization of a non-equilibrium sodiation pathway in copper sulfide, Nat. Commun. 9 (2018) 922, https://doi.org/10.1038/s41467-018-03322-9.

[42] L. Zhang, Y. Tang, Y. Wang, Y. Duan, D. Xie, C. Wu, L. Cui, Y. Li, X. Ning, Z. Shan, In situ TEM observing structural transitions of MoS$_2$ upon sodium insertion and extraction, RSC Adv. 6 (2016) 96035–96038, https://doi.org/10.1039/C6RA18188K.

[43] J. Wang, Metal Sulfides for High-Performance Lithium-Ion and Sodium-Ion Battery Anodes, University of Maryland Libraries, Maryland, 2015, 123-123.

[44] Q. Wu, L. Jiao, J. Du, J. Yang, L. Guo, Y. Liu, Y. Wang, H. Yuan, One-pot synthesis of three-dimensional SnS$_2$ hierarchitectures as anode material for lithium-ion batteries, J. Power Sources 239 (2013) 89–93. https://www.sciencedirect.com/science/article/pii/S0378775313004540.

[45] Y.C. Zhang, Z.N. Du, K.W. Li, M. Zhang, Size-controlled hydrothermal synthesis of SnS$_{(2)}$ nanoparticles with high performance in visible light-driven photocatalytic degradation of aqueous methyl orange, Separ. Purif. Technol. 81 (2011) 101–107. https://www.sciencedirect.com/science/article/pii/S1383586611004114.

[46] M. Cruz, J. Morales, J.P. Espinos, J. Sanz, XRD, XPS and Sn-119 NMR study of tin sulfides obtained by using chemical vapor transport methods, J. Solid State Chem. 175 (2003) 359–365. https://www.sciencedirect.com/science/article/pii/S0022459603003293.

[47] H.W. Nesbitt, M. Scaini, H. Hochst, G.M. Bancroft, A.G. Schaufuss, R. Szargan, Synchrotron XPS evidence for Fe^{2+}-S and Fe^{3+}-S surface species on pyrite fracture-surfaces, and their 3D electronic states, Am. Mineral. 85 (2000) 850–857. https://pubs.geoscienceworld.org/msa/ammin/article-abstract/85/5-6/850/133745.

[48] X. Yu, A. Manthiram, Na$_2$S-Carbon nanotube fabric electrodes for room-temperature sodium-sulfur batteries, Chem. Eur J. 21 (2015) 4233–4237. https://onlinelibrary_wiley.gg363.site/doi/abs/10.1002/chem.201405344.

[49] N.P. Kondekar, M.G. Boebinger, E.V. Woods, M.T. McDowell, In situ XPS investigation of transformations at crystallographically oriented MoS$_2$ interfaces, ACS Appl. Mater. Interfaces 9 (2017) 32394–32404. https://pubs.acs.org/doi/abs/10.1021/acsami.7b10230.

[50] R.S. Smart, W.M. Skinner, A.R. Gerson, XPS of sulphide mineral surfaces: metal-deficient, polysulphides, defects and elemental sulphur, Surf. Interface Anal. 28 (1999) 101–105. https://onlinelibrary_wiley.gg363.site/doi/abs/10.1002/(SICI)1096-9918(199908)28:1%3C101::AID-SIA627%3E3.0.CO;2-0.

[51] Y. Fu, C. Zu, A. Manthiram, In situ-formed Li$_2$S in lithiated graphite electrodes for lithium-sulfur batteries, J. Am. Chem. Soc. 135 (2013) 18044–18047. https://pubs.acs.org/doi/abs/10.1021/ja409705u.

[52] L.S. Price, I.P. Parkin, A.M.E. Hardy, R.J.H. Clark, T.G. Hibbert, K.C. Molloy, Atmospheric pressure chemical vapor deposition of tin sulfides (SnS, Sn2S3, and SnS2) on glass, Chem. Mater. 11 (1999) 1792–1799, https://doi.org/10.1021/cm990005z.

[53] J. Wang, F. Lin, H. Jia, J. Yang, C.W. Monroe, Y. NuLi, Towards a safe lithium-sulfur battery with a flame-inhibiting electrolyte and a sulfur-based composite cathode, Angew. Chem. Int. Ed. 53 (2014) 10099–10104. https://onlinelibrary_wiley.gg363.site/doi/abs/10.1002/anie.201405157.

[54] A. Belsky, M. Hellenbrandt, V.L. Karen, P. Luksch, New developments in the Inorganic Crystal Structure Database (ICSD): accessibility in support of materials research and design, Acta Crystallogr. B 58 (2002) 364–369, https://doi.org/10.1107/S0108768102006948.

[55] S. Kirklin, J.E. Saal, B. Meredig, A. Thompson, J.W. Doak, M. Aykol, S. Rühl, C. Wolverton, The Open Quantum Materials Database (OQMD): assessing the accuracy of DFT formation energies, Npj Comput. Mater. 1 (2015) 15010, https://doi.org/10.1038/npjcompumats.2015.10.

[56] S. Grindy, B. Meredig, S. Kirklin, J.E. Saal, C. Wolverton, Approaching chemical accuracy with density functional calculations: diatomic energy corrections, Phys. Rev. B 87 (2013), 075150. https://link.aps.org/doi/10.1103/PhysRevB.87.075150.

[57] L. Wang, T. Maxisch, G. Ceder, Oxidation energies of transition metal oxides within the GGA+U framework, Phys. Rev. B 73 (2006), 195107. https://link.aps.org/doi/10.1103/PhysRevB.73.195107.

[58] V. Stevanović, S. Lany, X. Zhang, A. Zunger, Correcting density functional theory for accurate predictions of compound enthalpies of formation: fitted elemental-phase reference energies, Phys. Rev. B 85 (2012), 115104. https://link.aps.org/doi/10.1103/PhysRevB.85.115104.

[59] A. Watson, T. Markus, Thermodynamic Properties of Inorganic Materials, Springer, Berlin, Heidelberg, 1999.

[60] P. Nash, Thermodynamic Database, 2013. https://tptc.iit.edu/index.php/thermo-database.
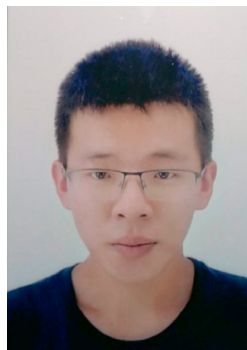
Mr. Zhongtao Ma received his Bachelor's degree from Northeastern University at China in 2016. He joined Prof. Anmin Nie and Prof. Qianqian Li's group in Shanghai University in Sept. 2016. He is especially interested in fabrication and characterization of energy material which can be applied in lithium-ion battery / all-solid-state battery.
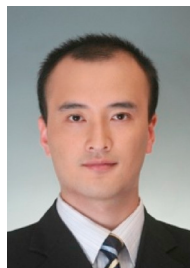
Dr. Zhenpeng Yao is a computational material scientist in the Department of Chemistry and Chemical Biology at Harvard University and Department of Chemistry and Department of Computer Science at University of Toronto. Zhenpeng conducts research focusing on a variety of phenomena observed in electrochemistry and searching for materials generally used in, yet not limited to, Li-ion batteries, including materials for anodes, cathodes, solid electrolytes, as well as Metal-organic Frameworks (MOFs). First-principles Density Functional Theory (DFT) Calculations, Monte Carlo Simulations, Non-equilibrium Phase Search Method, Nudged Elastic Band theory, and High-throughput/Machine Learning techniques are common tools used.

Dr. Yingchun Cheng received his B.Sc. and Ph.D. degrees from the Nanjing University in 2005 and 2010, respectively. He then conducted his postdoctoral research at the King Abdullah University of Science and Technology and the University of Illinois at Chicago from 2010 to 2015. He is now a full professor at the Institute of Advanced Materials, Nanjing Tech University. His research interests focus on the study of the electronic, optic, and magnetic properties of 2D materials and energy storage materials.

Mr. Xuyang Zhang is a master student at Institute of Advanced Materials in Nanjing Tech University. His research focuses on the calculation of defects in semiconductors.

Dr. Bingkun Guo is a professor in the Materials Genome Institute at Shanghai University, China. He received his PhD from the Institute of Physics, Chinese Academy of Sciences in 2009, which was followed by three years postdoctoral research at Oak ridge National Laboratory. After a postdoc at The University of Texas at Austin, he joined Shanghai University in 2015 and is working on synthesis of nanostructured materials for energy storage application and solid lithium ion batteries.

Dr. Yingchun Lyu is an associate professor in Materials Genome Institute, Shanghai University. He received his Ph.D degree in Condensed Matter Physics from Institute of Physics, Chinese Academy of Sciences in 2015. His researches focus on the energy storage mechanism of high energy density electrode materials for Li-ion and Na-ion batteries.

Dr. Wang Hongtao, professor and executive director of Center for X-Mechanics, Zhejiang University. He focuses on the development of instruments for the interdisciplinary research in fields of mechanics and material science. He has developed a 4-degree-freedom nano manipulator dedicated to both TEM tomography and in-situ TEM. A combination of the two methods can promote deeper understanding of microstructural evolution in 3D.

Dr. Peng Wang is an assistant professor in Materials Genome Institute at Shanghai University, Shanghai, China. He received his BS degree in Engineering Mechanics in 2011 and his Ph.D. degree in solid mechanics from Zhejiang University, Hangzhou, China. His has worked as a postdoctoral research associate in Zhejiang University and Georgia Institute of Technology from 2016 to 2018. His research focuses on the modeling and simulation of mechanical behavior of materials at the nano-to macroscale, developing new simulation method to capture new mechanism in alloy and other related structural materials, first-principle calculation in defects.
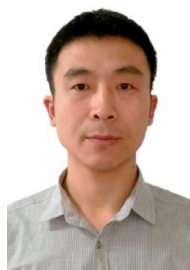
Dr Anmin Nie is a professor at Yanshan University. He received his Ph.D. in Solid Mechanics from Zhejiang University in 2012. During 2012–2016, he worked at Michigan Technological Univeristy and University of Illinois at Chicago as a post-doctoral research associate. His research interests are *in situ* microscopy on nano-scaled materials and their behaviors. He has published tens of papers in peer reviewed journals, such as *Science*, *Nano Letters*, and *ACS Nano*, et al.

Dr. Qianqian Li is an associate professor in Materials Genome Institute at Shanghai University. She received her BS degree in Materials Science and Technology from University of Jinan in 2009, and her Ph.D. degree in solid mechanics from Zhejiang University, China in 2014, and then followed to work as a postdoctoral research associate in NU*ANCE*, Department of Materials Science and Engineering, at Northwestern University, Evanston, IL, from 2014 to 2017. Her research area of interest includes *in-situ* transmission electron microscopy (TEM) technics, energy storage behaviors of electrodes for rechargeable batteries and supercapacitor, and synthesis and modification of functional materials.

Prof. Alán Aspuru-Guzik is a professor of chemistry and computer science at the University of Toronto. His research group studies machine learning, quantum computing, and automated chemistry. He is the chief scientific officer and founder of quantum computing startup Zapata Computing. Alán was an assistant professor at Harvard University since 2006, before becoming associate professor in 2010, and professor in 2013. In 2018, Professor Aspuru-Guzik moved to the University of Toronto as a Canada 150 Research Chair. Aspuru-Guzik had worked with Michael Aziz, Thomas Dudley Cabot, Roy Gordon and the United States Department of Energy to develop the grid-scale battery.